Molecular Engineering Accelerating Reverse Intersystem Crossing Endowed by Confining Donor to Ensure Low Efficiency Roll-Off OLEDs

Feng Wang, Song Zhao, Yali Peng, Yuqin Du, Huixia Xu,* Xinyu Li, Yanqin Miao,* Peng Tao,* and Hua Wang

ABSTRACT

To achieve stable organic light emitting diodes (OLEDs), great efforts are devoted to accelerating the reverse intersystem crossing (RISC) process of efficient thermally activated delayed fluorescence (TADF). Here, we focus on spin-orbit coupling engineering to increase the rate constant of RISC and the photoluminescence quantum yield (PLQY). Three TADF emitters consisting of a carbonyl carbazole core as the initially donor-acceptor system plus diphenylamine as the π-extended group were developed. We show that this design strategy realizes the fine adjustment of excited states to affect the spin-orbit coupling (SOC) matrix element between triplet and singlet states, resulting in accelerating k_{RISC} while maintaining high PLQYs and small ΔE_{ST}. OLEDs achieved excellent electroluminescence performance with a maximum external quantum efficiency of 23.8% and low efficiency roll-off, demonstrating great potential in efficient OLEDs.

INTRODUCTION

The organic light emitting diodes (OLEDs) have attracted increasing attention in the fields of full-color displays and lighting, which is attributed to their unique characteristics, such as flexibility, high brightness, low cost, etc. According to spin statistics, 75% of triplet excitons generated after carrier recombination were wasted by nonradiative decay because spin is forbidden for common fluorescent emitters. To fully utilize nonemissive triplet exciton, many emitting mechanisms have been proposed, such as phosphorescence, thermally activated delayed fluorescent (TADF), and hot-exciton emission. Compared with the other two mechanisms, TADF emitters can harvest both triplet and singlet exciton through a reverse intersystem crossing (RISC) process from the lowest triplet (T_1) to singlet (S_1) state to realize theoretically 100% internal quantum efficiency (IQE); thus, they are considered as the most promising candidates for commercial OLEDs. However, the roll-off efficiency at high brightness still restrict their development due to the slow RISC of long-lived triplet excitons.

Therefore, many researchers put their attention on the rate constant RISC (k_{RISC}) itself, while the relationships between the k_{RISC} and molecular engineering, which are critical for the development of high-performance OLEDs, are still rare reported.

Theoretically, the triplet excitons are obliged to undergo the $T_1 \rightarrow S_1 \rightarrow S_0$ processes to emit. The former process of $T_1 \rightarrow S_1$ strongly depends on k_{RISC} which should be maximized to accelerate triplet exciton upconversion to the singlet state. According to the first perturbation theory, a small energy gap (ΔE_{ST}) and a large spin-orbit coupling matrix element (SOCME) value between S1 and T1 are required for a fast RISC process. To obtain a small ΔE_{ST} to ensure efficient backward transfer to the S1 by thermal activation, most TADF emitters are generally designed with highly twisted donor (D)-acceptor (A) structures and completely separated distributions between the highest occupied molecular orbital (HOMO) and lowest unoccupied molecular orbital (LUMO). However, reduction through minimizing the exchange integral between the frontier orbitals also results in a reduced oscillator strength (f) and a large nonradiative of emissive S_1 state, which is in opposition to high photoluminescent quantum yield (PLQY). Thus, it is limited to boosting k_{RISC} by minimizing ΔE_{ST}.

SOCME between T_1 and S_1 deeply relies on triplet and singlet excited state characteristics. In D-A-type molecules, both S_1 and T_1 possess a dominant charge-transfer (CT) exciton character. This homologous excited state nature usually possess a negligible SOCME value (< 0.1 cm^{-1}), which produces inefficient RISC in spite of a small ΔE_{ST}. Their k_{RISC} values are usually 1-2 orders magnitude smaller than those of fluorescent materials with different orbital character. Consequently, severe roll-off in OLEDs at high brightness was observed due to the triplet exciton quenching. Emission from the predominantly CT singlet state (^{1}CT) via prompt or delayed fluorescence is desirable. Meanwhile, the triplet featuring a certain percentage local excitation (^{3}LE) facilitates a large SOCME value to prompt efficient exciton conversion to ^{1}CT.

Herein, we aim to design a series of highly efficient TADF materials with hybrid 3CT and 3LE T1 excitonic state to improve SOCME while keeping the CT-dominated S1 state. Carbonyl was chosen as electron-accepting group owing to its intrinsic n-π* transition, which was conducive to SOCME. The carbazole-benzophenone Cz2BP ($k_{RISC} = 1.5\times10^3$ s^{-1} and ΔE_{ST} = 0.21 eV) was used as D-A core to attain the ^{1}CT state. Additionally, Data et al. have shown that the introduction of multiple donor moieties could result in the formation of hybrid triplet state in D-A-type TADF molecules, and a small ΔE_{ST} for efficient triplet harvesting. The π-extended donors of diphenylamine

(DPA) were thus introduced. To reveal the effect of intramolecular interaction on photoluminescent properties, the electron-withdrawing pyridine ring was used to replace a benzene ring of benzophenone. As expected, the designed molecule exhibits a minimized ΔE_{ST} of 0.04 eV and an enhanced k_{RISC} of 1.5×10^6 s^{-1}, which is 3 orders of magnitude larger than that of the template molecule. Furthermore, an OLED based on these molecules achieves impressive electro-luminescent (EL) performance with a maximum external quantum efficiency (EQE) of 23.8% and very small efficiency roll-off.

According to the previous reports, the low PLQYs of carbonyl-based TADF materials were attributed to the rotations of benzene rings. Herein, the nitrogen atoms were introduced at the meta- and ortho-positions of keto to fix the molecular skeleton by intra- and intermolecular weak interactions. Meanwhile, the electron-withdrawing pyridine also can be used to regulate the LE percentages of T_1 sates, which also can open up additional RISC channels from the high-lying triplet, such as $T_2\rightarrow S_1$ to facilitate the spin-flip process. Three molecules (BDC, B2-DC, and B3-DC) were constructed in this work and are listed in Figure 1b. The details of the synthetic procedure are given in Scheme S1 (Supporting Information). The emitters of BDC, B2-DC, and B3-DC are feasibly obtained in mild conditions with high yields of 60-70% and fully characterized by ^{1}H NMR, ^{13}C NMR, and MS, as described in Figures S1-S8.

All target materials are thermally stable with high decomposition temperatures (T_d) of 563, 512, and 508 °C at 5% initial weight loss as determined by thermogravimetric analysis (TGA) and glass-transition temperatures (T_g) of 180, 181, and 173 °C as determined by differential scanning calorimetry (DSC), as shown in Figure S9. The HOMO levels of BDC, B2-DC, and B3-DC are measured to be -5.30, -5.31, and -5.32 eV, respectively, from electrochemical cyclic voltammetry (CV) measurements (Figure S10) and corresponding eq 1 in the Supporting Information.

Single crystals of B2-DC (CCDC 2370105) were obtained by slow diffusion of mixed dichloromethane/methanol solution. The crystal structures are outlined in Figure 1c, and corresponding data are summarized in Table S1. The weak intramolecular interactions between pyridine and the benzene ring of 2-benzoylpyridine are found with a N-H distance of 2.427 Å. DFT calculations show the intramolecular interaction of B2-DC is 2.3 Å for B2-DC, and the distance 2.4 Å between pyridine and the proximal C-H bonds of carbazole for B3-DC, which are marked as d1 and d2 respectively, in Figure 2a. The packing model of B2-DC is along a axis via C=O bonding to form six-petal-

blooming patterns with an X-type crossing without close π-π stacking, which is favorable for suppressing quenching at high exciton density.

Interaction region indicator (IRI) isosurface maps (isovalue of 1.05) and the electrostatic potential (ESP) mapped were calculated and shown in Figure S11. Both ortho- and meta-positions of keto exhibit the nearly neutral potential in BDC. When the N atom was introduced, the ESP of B2-DC and B3-DC exhibit the significant changes, suggesting the weak intramolecular interaction. However, there is no obvious hydrogen bonding from the RDG mapped isosurface, which should be marked in blue (Figure S11b). Therefore, the calculated results suggest that there is the weak intramolecular interaction between the N atom and proximate C-H, rather than hydrogen bonding. The potential energy surfaces (PESs) of BDC, B2-DC, and B3-DC also confirm these results (Figure S12).

The presence of a weak interaction and electron-withdrawing ability of pyridine is conducive to restrict intramolecular rotations and fix the molecular configurations. For example, the dihedral angle between pyridine and the benzene ring at the acceptor for B2-DC is 17.1°, which is much smaller than that of 29.9° in BDC. For B3-DC, the twisted angle between donors and pyridine ring is 35.8°, which is smaller than that of 48.3° in BDC. The root-mean-square displacement (RMSD) values on the S0 and S1 geometries of BDC, B2-DC, and B3-DC are 3.387, 2.133, and 2.256 Å, respectively, which also verified the above hypothesis (Figure S13). In a word, when the nitrogen atom is at the ortho-position of keto, the inner rotation of acceptor is suppressed. The rotations between donor and acceptor are confined when nitrogen atom is at meta-position of keto.

Their HOMOs are mainly distributed on carbazole and diphenylamine units, while LUMOs contribute to acceptors, showing more delocalization than that of reported Cz2BP (Figure 2a). The LUMO levels of 2-benzoylpyridine and 3-benzoylpyridine are 0.26 eV deeper than that of benzophenone (Figure S14). So, B2-DC and B3-DC thus possess deeper LUMO energy levels than BDC without nitrogen atoms, consistent with their more electron-deficient acceptor groups. The calculated HOMO levels of BDC, B2-DC, and B3-DC are −4.69, −4.63, and −4.71 eV, respectively. Consequently, the energy gaps (Eg) of B2-DC and B3-DC are smaller than that of BDC by 0.23 and 0.08 eV, respectively. B2-DC with a nitrogen atom at the ortho-position of keto exhibits a pronounced effect on LUMO levels. The main reason is that the meta-position is farther from the keto group than the ortho-position, and the inner rotation of 2-benzoylpyridine

is restricted in B2-DC to enhance the rigidity of the acceptor. The partial overlaps of HOMO and LUMO for BDC and B2-DC on pyridine and benzene rings offer the large oscillator strength f for S0 → S1 transitions of 0.1253 and 0.1601, respectively. The completely separated frontier orbital distributions of B2-DC lead to a smaller f of 0.0003.

The S_1 state energies of BDC, B2-DC, and B3-DC were calculated to be 2.56, 2.07, and 2.46 eV, while T_1 states were found to be 2.54, 2.06, and 2.45 eV, as shown in Figure 2b. Three materials show the small ΔE_{ST} values of 0.02, 0.01, and 0.01 eV, respectively, which can drive the RISC process, ultimately giving rise to TADF. Additionally, it is worth noting that the energy splitting between T_2 and T_1 for B2-DC (0.44 eV) is much larger than those of BDC (0.29 eV) and B3-DC (0.30 eV). Thus, the internal conversion (IC) from T_2 to T_1 is blocked for B2-DC, which is conducive to the PLQY. Meanwhile, the natural transition orbital (NTO) analysis reveals that S_1 states are dominated by CT characteristics with large CT/LE percentages (95.8/4.2 for BDC, 96.7/3.3 for B2- DC and 93.8/6.2 for B3-DC) (Figure 2c). The T_1 states of BDC and B3-DC exhibit large hole−particle overlaps, suggesting LE-dominated natures. These distinguishable different transition natures are attributed to the large SOC matrix element between T_1 and S_1 of 1.11 and 0.95 cm^{-1} for BDC and B3-DC, respectively.48 The T_1 state of B2-DC is dominated by a large CT percentage. This similar transition features between T_1 and S_1 result in a small SOCME of 0.09 cm^{-1}. Fortunately, the strong spin−orbit coupling between S_1 and T_2 with a SOCME value of 1.17 cm^{-1} accompanying the large energy splitting between T_2 and T_1 (0.44 eV) would drive the RISC process from T_2 to S_1. These distinct differences in excited states of BDC, B2-DC, and B3-DC imply the different photophysical properties.

The photophysical properties of BDC, B2-DC, and B3-DC were fully characterized in solution and aggregate film states. Three molecules show two main absorption bands in diluted toluene with a concentration of 1×10^{-5} M. The bands below 380 nm originated from the π−π* transitions of the conjugated skeleton and n-π* transitions of keto. The intramolecular CT states are reflected as absorption bands and extended to 430 nm (Figure 3a).49 BDC, B2-DC, and B3-DC show the maximum emission peaks at 552, 600, and 572 nm, respectively. From the absorption onsets, the optical gaps (Eg) of BDC, B2-DC, and B3-DC are estimated to be 2.62, 2.41, and 2.53 eV, respectively. Accompanying their HOMO energy levels from CV curves, the LUMO levels were calculated to be −2.68, −2.89 and −2.82 eV, respectively.

To confirm whether the π-extended donors have the effects on ΔEST, the fluorescence at 300 K and delayed phosphorescence spectra at 77 K of Cz2BP, BDC, B2-DC and B3-DC were measured in 2-MeTHF solution, as shown in Figure 3b. The S_1/T_1 energy levels of Cz2BP, BDC, B2-DC, and B3-DC were estimated to be 3.16/2.87, 3.10/2.89, 2.75/2.71, 2.58/ 2.54, and 2.70/2.64 eV, respectively. Thus, the corresponding ΔE_{ST} values of Cz2BP, BDC, B2-DC, and B3-DC are 0.29, 0.04, 0.04, and 0.06 eV, respectively. As expected, when the DPA is introduced on Cz2BP, the ΔE_{ST} is gradually decreasing due to the strong electron-donating ability. Additionally, the phosphorescence spectra of Cz2BP in 2-MeTHF with the delayed 1, 10, and 80 ms all show the fine structures, indicating a LE-dominated state (Figure S15). The phosphorescence Spectra of BDC, B2-DC, and B3-DC are all structureless, suggesting the large CT state. Transient PL spectra of three emitters exhibit single-exponential decay with nanosecond lifetimes, which could be attributed to fast nonradiative decay processes in diluted toluene solutions.

To further investigate their luminescent behaviors in aggregate states, BDC, B2-DC, and B3-DC were doped in the host of 4,4' bis(9-carbazoly)-1,1'-biphenyl (CBP) with various concentrations of 5, 10, 15, and 100 wt%. As depicted in Figure 3c and d, with the increasing doping concentrations, the CT emission spectra of the three emitters show progressive redshifts. From 5 wt% doped films to neat films, the emission peaks are red-shifted from 516 to 559 nm for BDC, from 548 to 592 nm for B2-DC, and from 542 to 573 nm for B3-DC due to concentration effects. The normalized PL spectra with different doping concentrations are shown in Figure S16. Meanwhile, their PLQYs show the different change trends with the increasing doping concentration: increasing from 71.8% (5 wt%) to 89.3% (10 wt%) and then falling to 33.0% (neat film) for BDC, decreasing from 50.1% (5 wt%) to 8.52% (neat film) for B2-DC, and decreasing from 71.8% (5 wt%) to 22.7% (neat film) for B3-DC (in Figure 3c and d). B2-DC and B3-DC exhibit lower PLQYs and stronger concentration dependence, which contribute to the smaller twisted structures. The low PLQY of B2-DC is mainly attributed to the small values of SOC and f. Consequently, the optimum doping concentrations of BDC, B2-DC, and B3-DC in CBP are 5, 5, and 10 wt%.

Subsequently, we recorded the transient PL decay spectra on BDC, B2-DC, and B3-DC with optimum doping concentrations in CBP (BDC: 10 wt%, B2-DC: 5 wt% and B3-DC: 5 wt%) at room temperature. As shown in Figure 3e, these films all show the double-exponential decays with promoted lifetimes (τ_p) of 8.34, 6.45, and 9.33 ns

from $S_1 \rightarrow S_0$ processes and delayed lifetimes (τ_d) of 1.2, 0.5, and 0.3 μs respectively. The delayed lifetimes are very short, manifesting the accelerated RISC process. Their temperature-dependent transient PL decay curves also clearly show typical TADF behaviors with increasing delayed fluorescence (Figure S17). The RISC rate constant (k_{RISC}), intersystem crossing rate constant (k_{ISC}), and radiative and nonradiative rate constants (k_r, k_{nr} respectively) were estimated according to the reported methods. As shown in Figure 4d, high k_r values on the order of 10^7 s^{-1} are achieved (Figure 3f). The k_{RISC} values of BDC, B2-DC, and B3-DC were calculated to be 3.5×10^6, 1.0×10^6 and 3.1×10^6 s^{-1}, respectively, which are larger than those of typical TADF molecules ($\approx10^4$–10^5). Especially, the k_r of BDC is two orders larger than k_mr ($\sim10^6$ s^{-1}), which is contributed to a high PLQY. Although B2-DC possesses a higher SOC value between T_2 and S_1, it exhibits a lower k_{RISC} and relatively low PLQY. On the one hand, the large energy split between T_2 and T_1 suppresses the IC process. On the other hand, the similar transition characteristic between T_2 and S_1 is not favorable for RISC.

Employing three molecules of BDC, B2-DC, and B3-DC as emitters and CBP as the host, simple devices were fabricated with the following structures: ITO/MoO_3 (30 nm)/TCTA (10 nm)/EML/TPBi (45 nm)/LiF/Al, in which the light-emitting layer (EML) is composed of the corresponding neat films or doped films in the CBP host (10 wt% BDC in CBP, 5 wt% B2-DC in CBP, and 5 wt% B3-DC in CBP). Indium tin oxide (ITO) and Al were used as the anode and cathode, and MoO_3 [4-(carbazol-9-yl)phenyl]amine (TCTA), 3,5-tris(1-phenyl-1H-benzimidazol-2-yl)benzene (TPBi), and lithium fluoride (LiF) were used as hole-injection, hole-transport, electron-transport, and hole-injection materials, respectively. The energy level diagrams and molecular structures of each layers were shown in Figure 4a. The nondoped devices based on BDC, B2-DC, and B3-DC exhibit the maximum emission peaks at 560, 611, and 592 nm, respectively. The device based on BDC achieves the best performances among all nondoped devices with a low turn-on voltage (at 1 cd/m²) of 2.7 V, a maximum luminance of L_{max} of 17460 cd/m², a maximum EQE (EQE_{max}) of 8.73%, a maximum power efficiency (PE_{max}) of 15.29 lm/W, and a maximum current efficiency (CE_{max}) of 16.64 cd/A (Figure S18).

In accord with the superior photophysical performance of the doping film compared to neat films, the doped devices were further investigated using CBP as the host with the concentrations of 5, 10, and 15 wt% (Figures S19-S21). Like the photophysical properties in the film, the optimized doping concentrations in devices were also 10, 5, and 5 wt% and are described in Figure 4. Their EL spectra display the

maximum emission peaks at 525, 561, and 547 nm, consistent with the PL spectra, indicating effective carrier transport and complete exciton recombination. According to the current density and luminance versus voltage (J-V-L) curves in Figure 4c, the low turn-on voltages (V_{on}) suggested a good carrier mobility in the devices. The L_{max} values of devices based on BDC, B2-DC, and B3-DC are 36740, 31290, and 38820 cd/m², respectively, which are obviously higher than that of nondoped devices. With a high PLQY, large k_r and small k_{nr}, BDC exhibits good electroluminescence performance with CE_{max}, PE_{max} and EQE_{max} values of 48.4 cd/A, 43.2 lm/W and 23.7% respectively, which are significantly higher than those of previous BTC (EQE_{max} = 7.6%).

Additionally, its EQE at 1000 cd/m² still remains 19.9% corresponding to a very small efficiency roll-off of 16.3%. The EQE_{max} values of devices based on BDC with the different doping concentrations of 5, 10, and 15 wt% are 21.9%, 23.7% and 21.7% respectively, showing the good doping concentration stability. The B3-DC-based devices also achieve excellent EL performance with an EQE_{max} of 20.6% and PE_{max} of 39.6 lm/W. B2-DC show relatively inferior performance with CE_{max}, PE_{max} and EQE_{max} of 32.3 cd/A, 27.4 lm/W and 17.3% respectively, as the photophysical properties. The EL performances of all devices in this work are all superior to the reported Cz2BP and BTC-based devices, indicating that our design strategy is effective to enhance the efficiency and stability for OLEDs.

In summary, three TADF emitters of BDC, B2-DC, and B3-DC with a fast RISC process have been successfully designed and comprehensively characterized based on theoretical calculations and photophysical measurements to elucidate the effects of chemical structure modification on the emission properties and device performances. Compared with the reported benzophenone-based TADF emitters, our BDC exhibits a smaller ΔE_{ST} of 0.04 eV, a larger SOC matrix element of 1.77 cm^{-1}, and a faster k_{RISC} of 1.5×10^6 s^{-1}. Upon doping with 10 wt% BDC in CBP hosts, the film displays an emission peak at 516 nm and a high PLQY of 89.3%. The emitters of B2-DC and B3-DC show the PLQYs of 50.1% and 61.8% and large k_{RISC} 3.1×10^6 and 3.9×10^6 s^{-1}. Benefitting from the above, the device based on BDC achieves superior EL performance with the maximum CE, PE, and EQE values of 48.4 cd/A, 43.2 lm/W and 27.8%.

Table 1. EL Performances of Devices Based on BDC, B2-DC, and B3-DC

emitter	x^a (wt %)	$V_{on}{}^b$ (V)	λ_{max} (nm)	$L_{max}{}^c$ (cd/m^2)	$CE_{max}{}^d$ (cd/A)	$PE_{max}{}^e$ (lm/W)	$EQE_{max}{}^f$/1000 (%)	roll-off^g (%)	CIE (x, y)
BDC	5	3.3	521	11700	44.0	34.6	21.9/17.9	18.0	(0.33, 0.54)
	10	3	525	36740	48.6	43.2	23.9/19.9	16.6	(0.34, 0.54)
	15	2.7	532	31610	44.2	44.3	21.7/20.2	6.6	(0.36, 0.54)
	nondoped	2.7	560	17460	16.6	15.3	8.7/8.7		(0.43, 0.53)
B2-DC	5	3	561	31290	32.3	27.4	17.3/13.7	20.9	(0.43, 0.52)
	10	3	570	28710	23.2	20.0	13.23/11.5	12.2	(0.46, 0.51)
	15	2.7	579	23550	18.5	17.5	11.2/10.1	9.9	(0.49, 0.50)
	nondoped	3	611	5420	2.5	2.2	2.3/1.9	19.2	(0.56, 0.43)
B3-DC	5	3	547	38820	41.0	39.6	20.6/18.2	11.5	(0.41, 0.54)
	10	3	553	37680	21.4	10.9	12.7/9.8	22.8	(0.41, 0.54)
	15	2.7	555	30530	24.0	15.3	14.1/12.0	15.1	(0.41, 0.53)
	nondoped	2.7	592	12220	7.1	7.0	4.6/4.4	2.6	(0.51, 0.48)

[a]Doping concentration. [b]Voltage at 1 cd/m^2. [c]The maximum luminance. [d]The maximum current efficiency. [e]The maximum power efficiency. [f]The maximum EQE/EQE at the 1000 cd/m^2. [g]The roll-off value at 1000 cd/m^2.

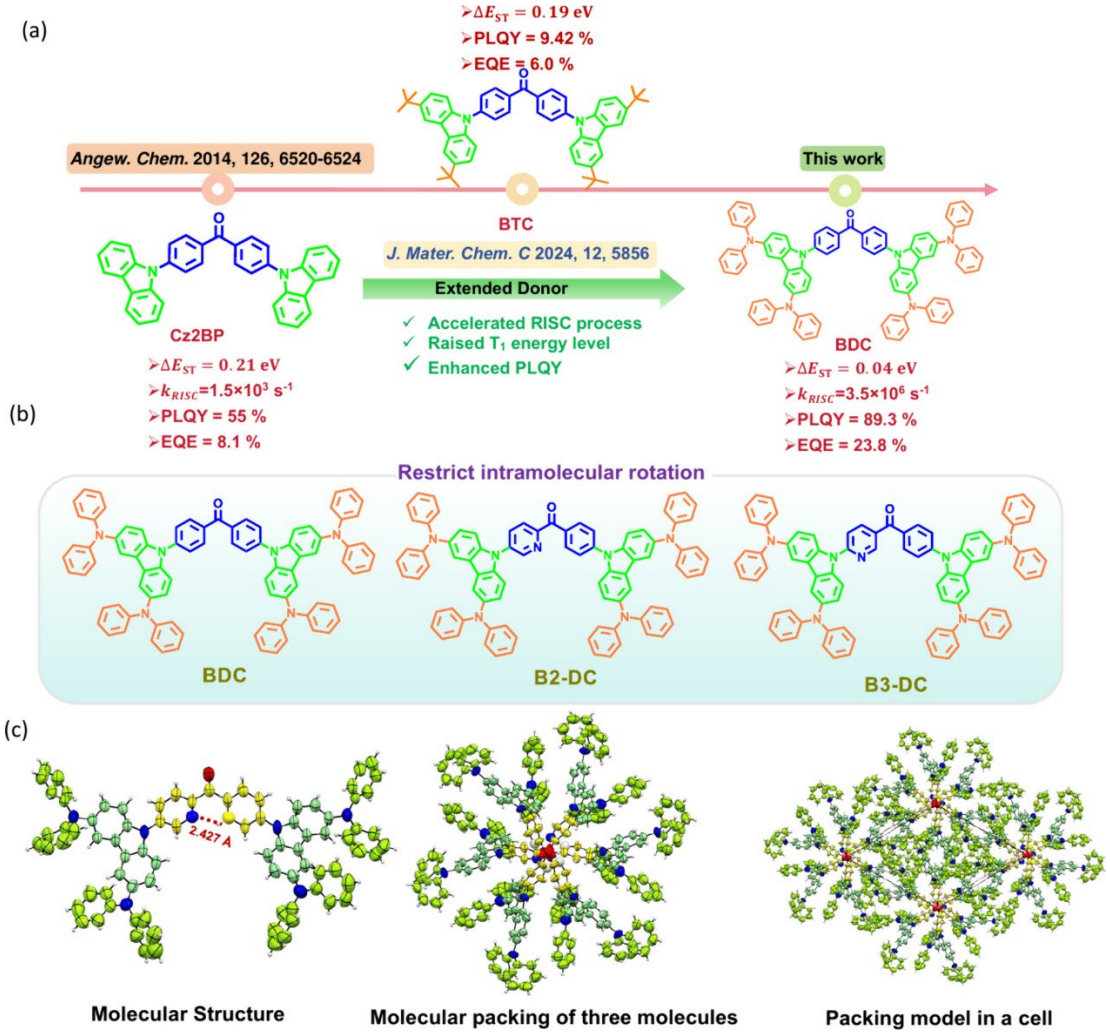

Figure 1. (a) Design strategy of TADF emitters based on benzophenone. (b) Molecular structures of BDC, B2-DC, and B3-DC. (c) Single crystal structures and packing of B2-DC.

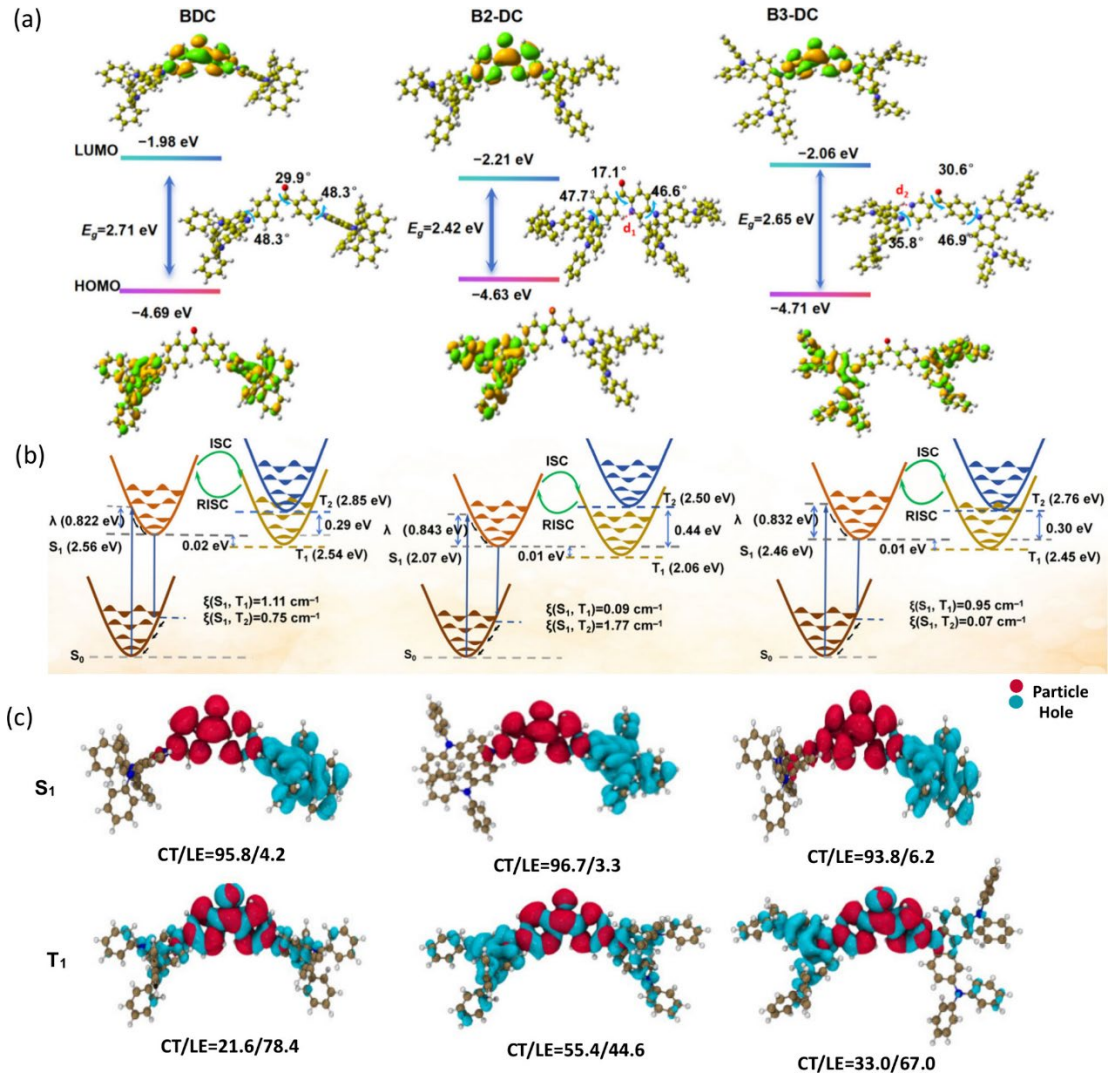

Figure 2. (a) Optimized molecular structures, calculated orbital distributions and energy levels of the HOMO and LUMO. (b) Energy level alignments and photophysical process of excited states. (c) NTO distributions and CT/LE proportions for S1 and T1 states of BDC, B2-DC, and B3-DC.

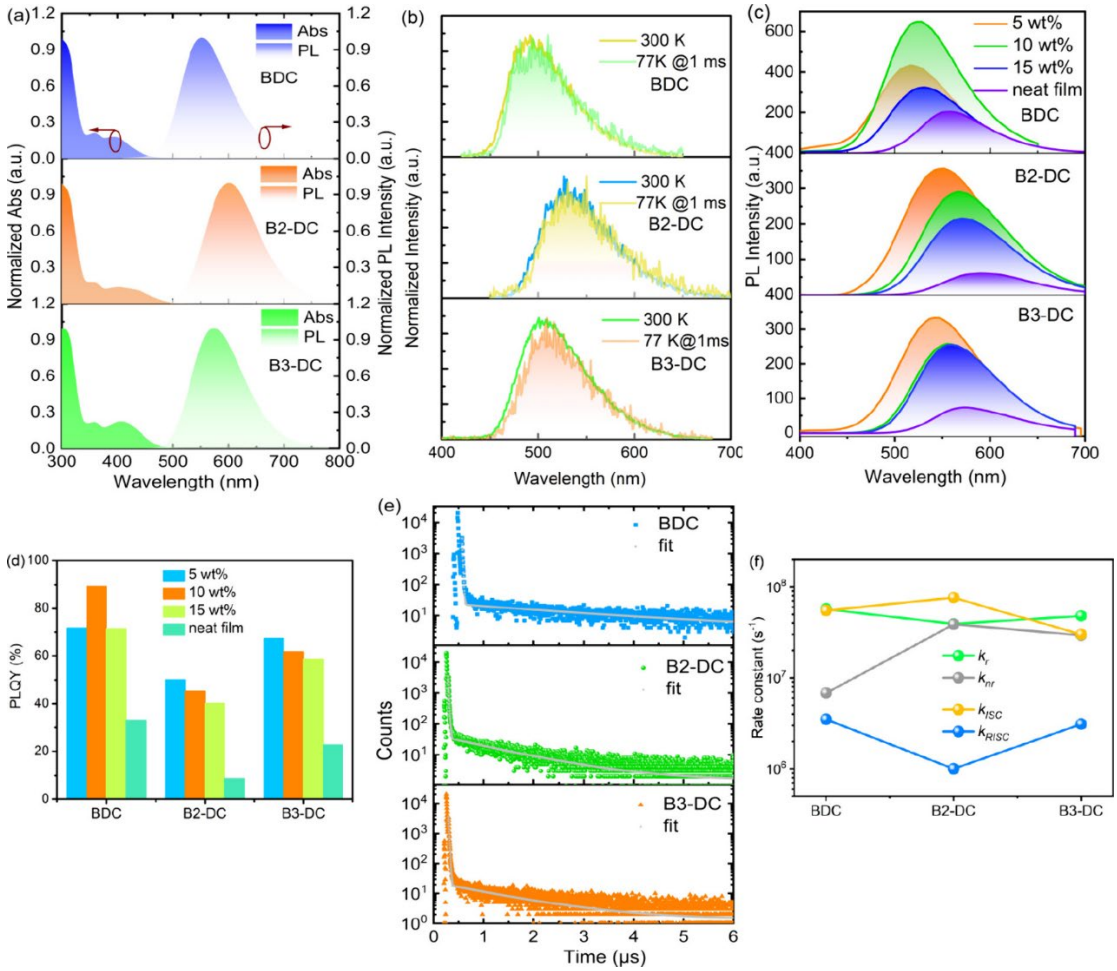

Figure 3. (a) Absorption and PL spectra in dilute toluene with the concentration of 1 × 10^{-5} M, (b) low-temperature phosphorescence and fluorescent spectra in 2-MeTHF solution, (c) PL spectra of films in CBP with different concentrations, (d) PLQYs of films with different doping concentrations, (e) transient PL decay in CBP with the optimum concentrations, and (f) rate constants of doping films of optimum concentrations in CBP of BDC, B2-DC and B3-DC.

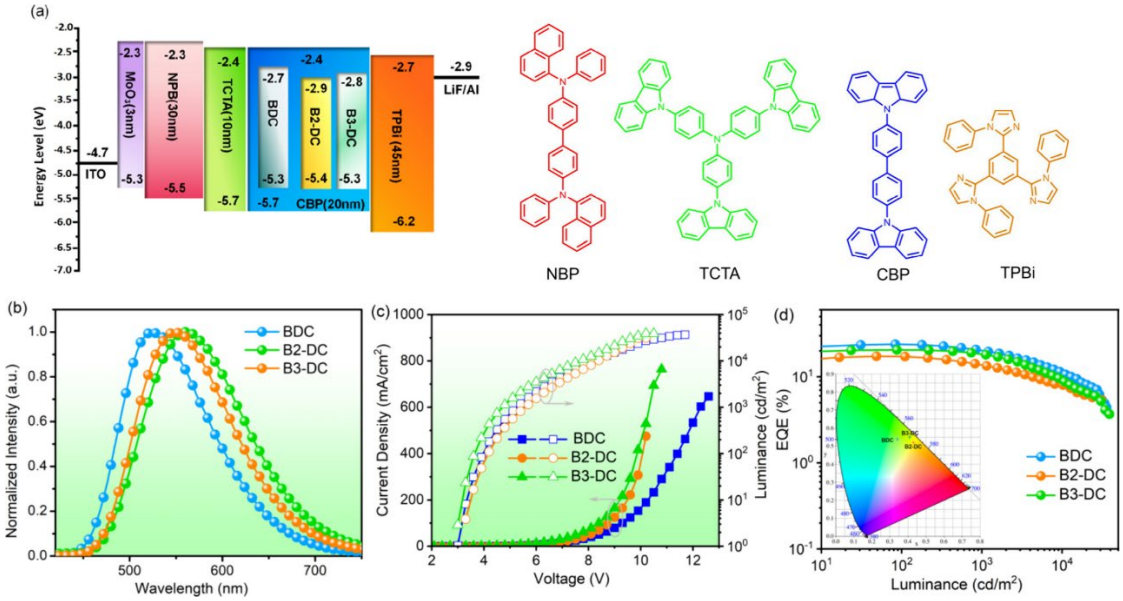

Figure 4. (a) Device structure, energy diagram, and molecular structures of each layer. (b) EL spectra at voltage of 5 V. (c) Current density–voltage-luminance curves and (d) external quantum efficiency versus luminance plots, CIE coordinates (insert) of doping devices for BDC, B2-DC, and B3-DC in CBP with optimal concentrations.

AUTHOR INFORMATION

Corresponding Authors

Huixia Xu – Key Laboratory of Interface Science and Engineering in Advanced Materials, Ministry of Education, Taiyuan University of Technology, Taiyuan 030024, China; orcid.org/0000-0003-0207-7039; Email: xuhuixia@tyut.edu.cn

Yanqin Miao – Key Laboratory of Interface Science and Engineering in Advanced Materials, Ministry of Education, Taiyuan University of Technology, Taiyuan 030024, China; orcid.org/0000-0003-2659-7696; Email: miaoyanqin@tyut.edu.cn

Peng Tao – Department of Applied Biology and Chemical Technology and Research Institute for Smart Energy, The Hong Kong Polytechnic University, Hong Kong 999077, P. R. China; orcid.org/0000-0003-1932-557X; Email: pengtao@polyu.edu.hk

Authors

Feng Wang – Key Laboratory of Interface Science and Engineering in Advanced Materials, Ministry of Education, Taiyuan University of Technology, Taiyuan 030024, China

Song Zhao – Key Laboratory of Interface Science and Engineering in Advanced

Materials, Ministry of Education, Taiyuan University, of Technology, Taiyuan 030024, China
Yali Peng – Key Laboratory of Interface Science and Engineering in Advanced Materials, Ministry of Education, Taiyuan University of Technology, Taiyuan 030024, China
Yuqin Du – Key Laboratory of Interface Science and Engineering in Advanced Materials, Ministry of Education, Taiyuan University of Technology, Taiyuan 030024, China
Xinyu Li – Key Laboratory of Interface Science and Engineering in Advanced Materials, Ministry of Education, Taiyuan University of Technology, Taiyuan 030024, China
Hua Wang – Key Laboratory of Interface Science and Engineering in Advanced Materials, Ministry of Education, Taiyuan University, of Technology, Taiyuan 030024, China; orcid.org/0000-0002-2976-9521

Author Contributions

The manuscript was written through contributions of all authors. All authors have given approval to the final version of the manuscript. Feng Wang drafted the manuscript. Xinyu Li fabricated and characterized the OLED devices; Song Zhao synthesized and characterized the compounds; Yali Peng measured the PL spectra; Yanqin Miao provided the investigation, methodology, and validation; and Yuqin Du analyzed the data and corrected the manuscript.

Notes

The authors declare no competing financial interest.

ACKNOWLEDGMENTS

This work was financially supported by the Joint Funds of the National NSFC (U21A20492), the National Natural Science Foundation of China (62074109), the Key R&D program of Shanxi Province (International Cooperation, 201903D421087, 201903D121100), the Science and Technology Innovation Talent Team Project of Shanxi Province (202204051001013), and the Fund Program for the Scientific Activities of Selected Returned Overseas Professionals in Shanxi Province (20230007).

REFERENCES

(1) Feng, Q.; Zhu, S.; Wang, B.; Yu, F.; Li, H.; Yu, M.; Xu, M.; Xie, L. Thermally activated delayed fluorescence macrocycles for organic light-emitting diodes. Adv. Funct. Mater. 2024, 34, 2312622.

(2) Li, W.; Li, M.; Li, W.; Xu, Z.; Gan, L.; Liu, K.; Zheng, N.; Ning, C.; Chen, D.; Wu, Y. C.; Su, S. J. Spiral donor design strategy for blue thermally activated delayed fluorescence emitters. ACS Appl. Mater. Interfaces. 2021, 13, 5302-5311.

(3) Meng, Q.; Wang, R.; Wang, Y.; Guo, X.; Liu, Y.; Wen, X.; Yao, C.; Qiao, J. Longevity gene responsible for robust blue organic materials employing thermally activated delayed fluorescence. Nat. Commun. 2023, 14, 3927.

(4) Yang, H.; Zheng, J.; Xie, M.; Luo, D.; Tang, W. J.; Peng, S. K.; Cheng, G.; Zhang, X.; Zhou, X. P.; Che, C. M.; Li, D. Aggregation-enhanced emission in a red Cu(I) emitter with quantum yield > 99%. ACS Mater. Lett. 2022, 4, 1921-1928.

(5) Agou, T.; Matsuo, K.; Kawano, R.; Park, I. S.; Hosoya, T.; Fukumoto, H.; Kubota, T.; Mizuhata, Y.; Tokitoh, N.; Yasuda, T. Pentacyclic ladder-heterobarin emitters exhibiting high-efficiency blue thermally activated delayed fluorescence with an ultrashort emission lifetime. ACS Mater. Lett. 2020, 2, 28-34.

(6) Jin, J.; Duan, C.; Jiang, H.; Tao, P.; Xu, H.; Wong, W. Y. Integrating Asymmetric O-B-N unit in Multi-Resonance thermally activated delayed fluorescence emitters towards High-Performance deep-blue organic light-emitting diodes. Angew. Chem., Int. Ed. 2023, 62, No. e202218947.

(7) Tao, P.; Lu, X.; Zhou, G.; Wong, W. Y. Asymmetric Tris-Heteroleptic cyclometalated phosphorescent Iridium(III) complexes: An emerging class of metallophosphors. Acc. Mater. Res. 2022, 3, 830-842.

(8) Tao, P.; Lv, Z.; Zheng, X. K.; Jiang, H.; Liu, S.; Wang, H.; Wong, W. Y.; Zhao, Q. Isomer engineering of lepidine-Based Iridophosphors for far-Red hypoxia imaging and photodynamic therapy. Inorg. Chem. 2022, 61, 17703-17712.

(9) Tao, P.; Lv, Z.; Zhao, F. Q.; Zheng, X. K.; Jiang, H.; Li, W.; Deng, Y.; Liu, S.; Xie, G.; Wong, W. Y.; Zhao, Q. One-Pot synthesis of acetylacetone-based isomeric phosphorescent cyclometalated Iridium(III) complexes via random cyclometalation: A strategy for excited-state manipulation. Inorg. Chem. 2023, 62, 1202-1209.

(10) Endo, A.; Ogasawara, M.; Takahashi, A.; Yokoyama, D.; Kato, Y.; Adachi, C. Thermally activated delayed fluorescence from Sn4-Porphyrin complexes and their application to organic light emitting diodes - a novel mechanism for

electroluminescence. Adv. Mater. 2009, 21, 4802-4806.
(11) Uoyama, H.; Goushi, K.; Shizu, K.; Nomura, H.; Adachi, C. Highly efficient organic light-emitting diodes from delayed fluorescence. Nature. 2012, 492, 234-238.
(12) Luo, Q.; Gao, Y.; Xu, H.; Zhao, S.; Dong, W.; Miao, Y.; Wang, T.; Wang, H.; Yu, J. Applications of hot-exciton anthracene and imidazole derivatives in integrated organic blue-emitting diodes and ultraviolet photodetectors. J. Mater. Chem. C 2023, 11, 15918-15925.
(13) Dong, W.; Bai, Y.; Wang, Y.; Zhao, S.; Xu, H.; Miao, Y.; Luo, Q.; Wang, H.; Yu, J. Utilizing anthracene- and triphenylamine-based blue fluorescent emitters with D-π-A structures in integrated organic light-emitting and ultraviolet photodetector devices. Sci. China Mater. 2024, 67, 197-204.
(14) Xu, Y.; Liang, X.; Zhou, X.; Yuan, P.; Zhou, J.; Wang, C.; Li, B.; Hu, D.; Qiao, X.; Jiang, X.; et al. Highly efficient blue fluorescent OLEDs based on upper level triplet-singlet intersystem crossing. Adv. Mater. 2019, 31, 1807388.
(15) Dias, F.; Bourdakos, K. N.; Jankus, V.; Moss, K. C.; Kamtekar, K. T.; Bhalla, V.; Santos, J.; Bryce, M. R.; Monkman, A. P. Triplet harvesting with 100% efficiency by way of thermally activated delayed fluorescence in charge transfer OLED emitters. Adv. Mater. 2013, 25, 3707-3714.
(16) Ochi, J.; Yamasaki, Y.; Tanaka, K.; Kondo, Y.; Isayama, K.; Oda, S.; Kondo, M.; Hatakeyama, T. Highly efficient multi-resonance thermally activated delayed fluorescence material toward a BT-2020 deep-blue emitter. Nat. Commun. 2024, 15, 2361.
(17) Gillett, A.; Pershin, A.; Pandya, R.; Feldmann, S.; Sneyd, A.; Alvertis, A.; Evans, E.; Thomas, T.; Cui, L. S.; Drummond, B.; Scholes, G.; Olivier, Y.; Rao, A.; Friend, R.; Beljonne, D. Dielectric control of reverse intersystem crossing in thermally activated delayed fluorescence emitters. Nat. Mater. 2022, 21, 1150-1157.
(34) Rajamalli, P.; Chen, D.; Li, W.; Samuel, I. D. W.; Cordes, D. B.; Slawin, A. M. Z.; Zysman-Colman, E. Enhanced thermally activated delayed fluorescence through bridge modification in sulfone-based emitters employed in deep blue organic light-emitting diodes. J. Mater. Chem. C 2019, 7, 6664-6671.
(35) Haykir, G.; Aydemir, M.; Danos, A.; Gumus, S.; Hizal, G. H.; Monkman, A. P.; Turksoy, F. Effects of symmetric acceptor and donor positioning in deep blue pyridyl-sulfonyl based TADF emitters. Dyes & Pigments 2021, 194, 109579.
(36) Zhao, S.; Yang, T.; Xu, H.; Wang, F.; Peng, Y.; Du, Y.; Chen, K.; Miao, Y.; Wang,

H. Realization of highly efficient organic emitting diodes using thermally activated delayed fluorescence materials with fast reverse intersystem crossing. J. Mater. Chem. C 2024, 12, 5856-5863.
(37) Fu, Y.; Liu, H.; Yang, D.; Ma, D.; Zhao, Z.; Tang, B. Boosting external quantum efficiency to 38.6% of sky-blue delayed fluorescence molecules by optimizing horizontal dipole orientation. Sci. Adv. 2021, 7, No. eabj2504.
(38) Zhang, D.; Suzuki, K.; Song, X.; Wada, Y.; Kubo, S.; Duan, L.; Kaji, H. Thermally activated delayed fluorescent materials combining intra- and intermolecular charge transfers. ACS Appl. Mater. Interfaces. 2019, 11, 7192-7198.
(39) Wang, J.; Yang, Y.; Gu, F.; Zhai, X.; Yao, C.; Zhang, J.; Jiang, C.; Xi, X. Molecular engineering modulating the singlet-triplet energy splitting of indolo-carbazole-based TADF emitters exhibiting AIE properties for nondoped blue OLEDs with EQE of nearly 20%. ACS Appl. Mater. Interfaces. 2023, 15, 59643-59654.
(40) Thangaraji, V.; Rajamalli, P.; Jayakumar, J.; Huang, M. J.; Chen, Y. W.; Cheng, C. H. Quinolinylmethanone-based thermally activated delayed fluorescence emitters and the application in OLEDs: effect of intramolecular H-bonding. ACS Appl. Mater. Interfaces. 2019, 11, 17128-17133.
(41) Hempe, M.; Kukhta, N. A.; Danos, A.; Batsanov, A. S.; Monkman, A. P.; Bryce, M. R. Intramolecular hydrogen bonding in thermally activated delayed fluorescence emitters: is there evidence beyond reasonable doubt. J. Phys. Chem. Lett. 2022, 13, 8221-8227.
(42) Hojo, R.; Bergmann, K.; Hudson, Z. M. Investigating hydrogen bonding in quinoxaline-based thermally activated delayed fluorescent materials. J. Phys. Chem. Lett. 2024, 15, 5600-5606.
(43) Bergmann, K.; Hojo, R.; Hudson, Z. M. Uncovering the mechanism of thermally activated delayed fluorescence in coplanar emitters using potential energy surface analysis. J. Phys. Chem. Lett. 2023, 14, 310-317.
(44) Chen, D.; Huang, R.; Batsanov, A.; Pander, P.; Hsu, Y. T.; Chi, Z.; Dias, F.; Bryce, M. Intramolecular charge transfer controls switching between room temperature phosphorescence and thermally activated delayed fluorescence. Angew. Chem., Int. Ed. 2018, 57, 16407-16411.
(45) Noda, H.; Chen, X.-K.; Nakanotani, H.; Hosokai, T.; Miyajima, M.; Notsuka, N.; Kashima, Y.; Bredas, J.-L.; Adachi, C. Critical role of intermediate electronic states for spin-flip processes in charge-transfer-type organic molecules with multiple donors and

acceptors. Nat. Mater. 2019, 18, 1084-1090.
(46) Ma, H.; Peng, Q.; An, Z.; Huang, W.; Shuai, Z. Efficient and long-lived room-temperature organic phosphorescence: theoretical descriptors for molecular designs. J. Am. Chem. Soc. 2019, 141, 1010-1015.
(47) Bas, E.; Ulukan, P.; Monari, A.; Aviyente, V.; Catak, S. Photophysical Properties of benzophenone-based TADF emitters in relation to their molecular structure. J. Phys. Chem. A 2022, 126, 473-484.
(48) Rajamalli, P.; Senthilkumar, N.; Huang, P. Y.; Ren-Wu, C. C.; Lin, H. W.; Cheng, C. H. New molecular design concurrently providing superior pure blue, thermally activated delayed fluorescence and optical out-coupling efficiencies. J. Am. Chem. Soc. 2017, 139, 10948-10951.
(49) Huang, Z.; Xie, H.; Miao, J.; Wei, Y.; Zou, Y.; Hua, T.; Cao, X.; Yang, C. Charge transfer excited state promoted multiple resonance delayed fluorescence emitter for high-performance narrowband electroluminescence. J. Am. Chem. Soc. 2023, 145 (23), 12550-12560.
(50) Lee, J.; Jo, U.; Lee, J. Y. Suppression of dexter energy transfer through modulating donor segments of thermally activated delayed fluorescence assistant dopants. ACS Appl. Mater. Interfaces 2023, 15, 21261-21269.
(51) dos Santos, P. L.; Ward, J. S.; Congrave, D. G.; Batsanov, A. S.; Eng, J.; Stacey, J. E.; Penfold, T. J.; Monkman, A. P.; Bryce, M. R. Triazatruxene: A rigid central donor unit for a D-A3 thermally activated delayed fluorescence material exhibiting sub-microsecond reverse intersystem crossing and unity quantum yield via multiple singlet-triplet state pairs. Adv. Sci. 2018, 5, 1700989.
(52) Franca, L. G.; Danos, A.; Monkman, A. Spiro donor-acceptor TADF emitters: naked TADF free from inhomogeneity caused by donor acceptor bridge bond disorder. Fast rISC and invariant photophysics in solid state hosts. J. Mater. Chem. C 2022, 10, 1313.
(53) Kim, H. S.; Lee, J. S.; Shin, S.; Jeong, W.; Lee, S. H.; Kim, S.; Lee, J.; Suh, M. C.; Yoo, S. Enhancement of reverse intersystem crossing in charge-transfer molecule through internal heavy atom effect. Adv. Funct. Mater. 2021, 31, 2104646.